

Customizing Textile and Tactile Skins for Interactive Industrial Robots

Bo Ying Su* Zhongqi Wei* James McCann* Wenzhen Yuan*
Changliu Liu*

* *Carnegie Mellon University (emails: boyings, zhongqi2, jmccann, wenzheny, cliu6@andrew.cmu.edu)*

Abstract: Tactile skins made from textiles enhance robot-human interaction by localizing contact points and measuring contact forces. This paper presents a solution for rapidly fabricating, calibrating, and deploying these skins on industrial robot arms. The novel automated skin calibration procedure maps skin locations to robot geometry and calibrates contact force. Through experiments on a FANUC LR Mate 200id/7L industrial robot, we demonstrate that tactile skins made from textiles can be effectively used for human-robot interaction in industrial environments, and can provide unique opportunities in robot control and learning, making them a promising technology for enhancing robot perception and interaction.

Keywords: Textile and tactile skin, skin calibration, interactive industrial robots, human-robot interaction.

1. INTRODUCTION

Industrial robots usually perform precise and repetitive tasks, but are limited by highly structured and deterministic environments, hindering their flexibility. In order for robots to adapt to changing environments and perform unstructured tasks, it is critical to improve their interactivity. This paper introduces textile and tactile skins as a new sensing modality, and demonstrates their effectiveness in enhancing interactivity of industrial robots.

Robot control in interactive tasks heavily relies on available sensors. Six-axis Force Torque Sensors (FTS) can measure contact force and torque but cannot localize the contact position (Cao et al., 2021). Robot joint motor measurements can estimate external force and detect collisions, but do not localize the contact positions (Wahrburg et al., 2017). Vision-based systems can localize contact but do not detect force and suffer from occlusion (Kloss et al., 2020). Light curtains do not suffer from occlusion but can not be easily retrofitted onto complex geometries (Tsuji and Kohama, 2020). On the other hand, FTS can provide real-time data with high frequency, while vision-based systems are limited by the camera frame rate, typically 30 Hz or lower. FTS require professional installation, while vision-based systems are more portable but require significant calibration effort.

Tactile skins are a type of sensors that can be utilized in robots for a variety of control applications (Dahiya et al., 2013). Previous researchers have successfully developed tactile skins for human-robot interactive tasks (Cirillo et al., 2015; Baykas et al., 2020; Fan et al., 2022). However, these sensors are often not customizable and are difficult to adapt to different robots. Additionally, while some commercial skins, such as the T-skin (Touch Solution, 2023), are available to enhance robot safety, they are in general costly. Moreover, relying solely on basic safety

settings where robots stop upon skin contact may not be suitable for intricate human-robot interaction tasks.

Recently, a new type of flexible tactile skin using textiles called the Robot Sweater has been proposed (Si et al., 2023). These soft and deformable sensors can be easily deployed to various robots by creating customized knitting patterns. The tactile skin detects contact forces and can localize multiple contact positions. As it is attached directly to the robot surface, it is free from occlusion issues. The tactile skin provides real-time data with a high frequency of up to 150 Hz and is deformable and stretchable, making it easy to be deployed to different robots by adjusting its dimensions and tension to achieve a tight and robust fit to the robot surface, even with complex curvature.

However, these tactile skins have yet to be applied to industrial robots, which require higher precision in localization and pressure sensing for control applications. To address this gap, this paper presents a holistic solution for rapidly fabricating, calibrating, and deploying tactile skins to industrial robot arms. Our contributions are as follows: 1) we introduce a method for determining skin parameters based on robot geometry (Section 2); 2) we propose an automated skin calibration process that calibrates both the position and force reading from the skin to the robot (Section 3); and 3) we demonstrate how the skins can be integrated into robot control and learning to improve interactivity of industrial robots through experiments on a FANUC LR Mate 200id/7L industrial robot arm (Section 4).

2. SKIN FABRICATION

This section first reviews the principles and sensing mechanisms of the textile and tactile skin. We then discuss how to determine the appropriate skin parameters for different robots.

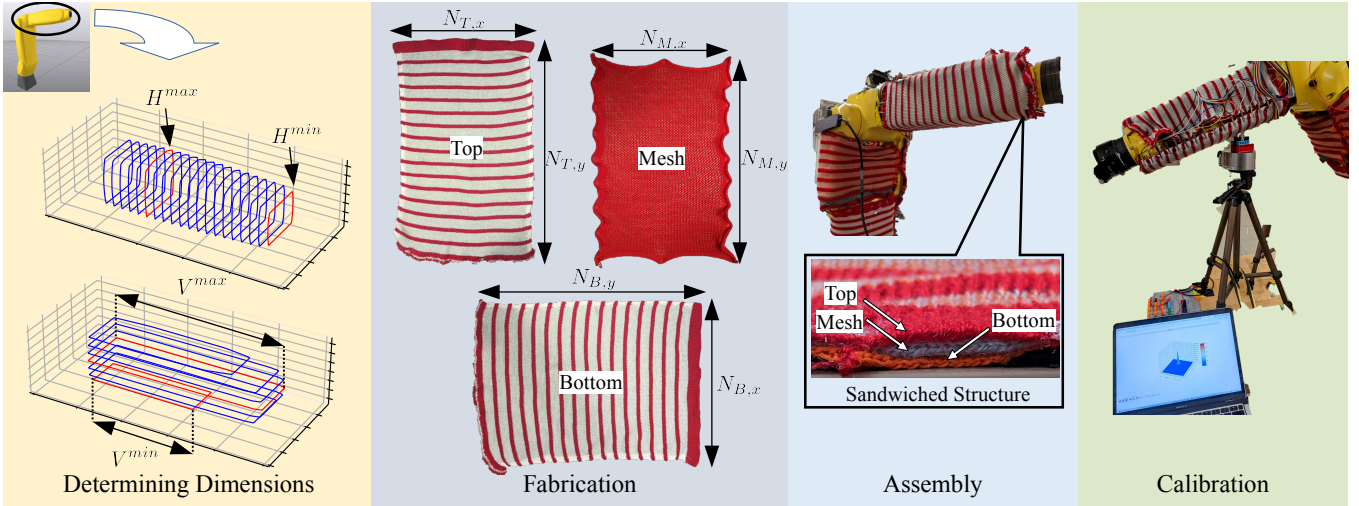


Fig. 1. The fabrication process for the textile and tactile skin. Firstly, the dimensions of the top, mesh, and bottom layers of the skin are determined by measuring H^{min} , H^{max} , V^{min} , and V^{max} from each link of the robot mesh. Next, the three layers of the skin are knitted and assembled by stacking them together to form a pressure-sensitive array. Finally, the skin is attached to the robot, and a calibration process is performed to determine the position and force responses of individual sensing cells.

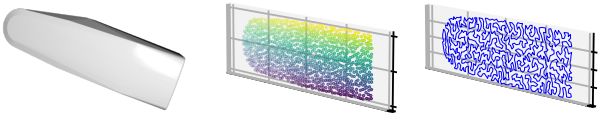


Fig. 2. Planning the skin calibration sequence. Firstly, the surface of the robot link is sampled from the mesh. Next, a trajectory is planned for the force-torque sensor to visit each sample on the surface. The robot executes the trajectory while the force-torque sensor records the force and torque at each sample point. The robot touches each location of the skin with varying pressure from 0N to 10N.

2.1 Principles of the Textile and Tactile Skin

As proposed by Si et al. (2023), the textile and tactile skin, Robot Sweater, consists of three layers of fabric in a sandwich structure, as shown in the assembly stage of Figure 1. The top and bottom layers contain alternating conductive and non-conductive stripes placed orthogonally, while the middle layer is formed by a mesh that separates the top and bottom layers. When pressure is applied to the skin, the top and bottom layers are stretched, causing the conductive stripes to touch each other and complete the circuit. The resistance, which is inversely correlated to the touching area of the top and bottom layers, is then recorded by an Arduino microcontroller. Once the skin parameters are determined, the skin can be automatically made by a knitting machine.

2.2 Determination of Skin Parameters

To successfully use tactile skins on industrial robot arms, we must choose the appropriate skin material and dimensions. We will explain how to determine these parameters for a given robot.

Skin Material In Si et al. (2023), Rayon yarn was used in the skin’s fabrication. In this work, we found that

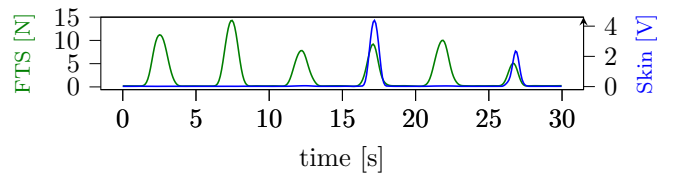


Fig. 3. Sample data collected during the calibration process for cell 80 of the tactile skin. The calibration process records force torque sensor readings, the robot’s joint angle, and the skin’s pressure readings simultaneously. This figure shows that certain points on the robot surface trigger a response from cell 80, while others do not. These responses allow us to localize the position of cell 80 on the robot surface.

acrylic yarn is more robust when attached to complex robot geometries due to its thickness and it being sturdier.

Skin Dimensions This work uses a flat rectangular skin to wrap around a cylinder-link object for ease of fabrication. For a cylinder-like object (shown in the first stage of Figure 1), we extract the following parameters: 1) the longest and shortest perimeters along the rotational x-axis: H^{max} and H^{min} ; 2) the maximum and minimum partial height along the orthogonal y-axis: V^{max} and V^{min} .

The parameters we need to choose are the number of columns (x) and rows (y) of the top (T), mesh (M), and bottom (B) layers of the skin, denoted by $N_{i,j} \in \mathbb{N}$, where $i \in T, M, B$ and $j \in x, y$. Note that the actual size of the skin layer i is determined by the stitch conversion ratio: $R_{i,x}$ (horizontal ratio) and $R_{i,y}$ (vertical ratio) for $i \in T, M, B$.¹ The non-stretched dimension of the skin layer i is $N_{i,x}/R_{i,x} \times N_{i,y}/R_{i,y}$.

¹ The stitch conversion ratio is 0.889 stitches/mm for the x-axis and 0.981 stitches/mm for the y-axis for the top and bottom layers, while it is 0.543 stitches/mm for the x-axis and 0.437 stitches/mm for the y-axis for the mesh layer.

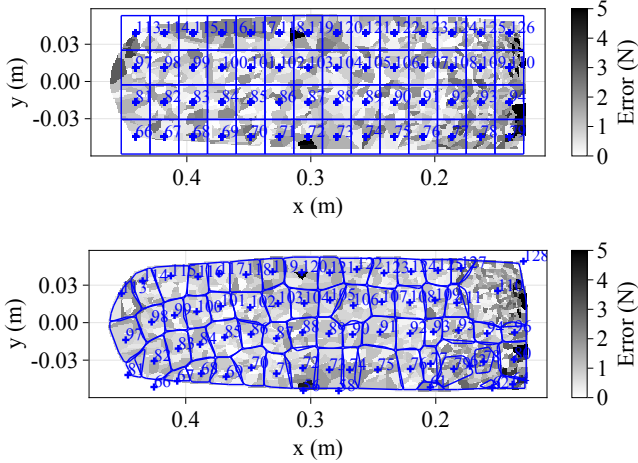


Fig. 4. Calibration result. The first plot shows the localization and force estimation error before calibration. The second plot shows the calibration result. The blue boundaries show the calculated receptive field of the sensing cells. The darker color represents a greater force estimation error compared to the ground truth.

Since the knitted skin has different stretchability along the horizontal and vertical axes, we define the maximum horizontal stretch as $\bar{S}_{i,x}$ and the maximum vertical stretch as $\bar{S}_{i,y}$ for $i \in \{T, M, B\}$. Meanwhile, to obtain reasonable conductivity on the conductive stripes as well as to tightly fit the cylinder-like object, the skin needs to be stretched to some extent. We define the minimum horizontal stretch as $\underline{S}_{i,x}$ and the minimum vertical stretch as $\underline{S}_{i,y}$ for $i \in \{T, M, B\}$.² Hence, the actual size of the skin layer i should be within $[N_{i,x}\underline{S}_{i,x}/R_{i,x}, N_{i,x}\bar{S}_{i,x}/R_{i,x}] \times [N_{i,y}\underline{S}_{i,y}/R_{i,y}, N_{i,y}\bar{S}_{i,y}/R_{i,y}]$. To let the skin fit the cylinder-like object, the following relationship needs to be satisfied $\forall i \in \{T, M, B\}$,

$$N_{i,x}\underline{S}_{i,x}/R_{i,x} \leq H^{min} \leq H^{max} \leq N_{i,x}\bar{S}_{i,x}/R_{i,x}, \quad (1a)$$

$$N_{i,y}\underline{S}_{i,y}/R_{i,y} \leq V^{min} \leq V^{max} \leq N_{i,y}\bar{S}_{i,y}/R_{i,y} \quad (1b)$$

In order to ensure feasibility of (1), the object must satisfy that $H^{max}/H^{min} \leq \min_{i \in \{T, M, B\}} \{\bar{S}_{i,x}/\underline{S}_{i,x}\}$ and $V^{max}/V^{min} \leq \min_{i \in \{T, M, B\}} \{\bar{S}_{i,y}/\underline{S}_{i,y}\}$, so that the maximum perimeter of the object falls within the skin's stretch tolerance.

Then we select the smallest dimension that satisfies (1), where for $i \in \{T, M, B\}$,

$$N_{i,x} = \lceil H^{min} R_{i,x} / \underline{S}_{i,x} \rceil \quad (2a)$$

$$N_{i,y} = \lceil V^{min} R_{i,y} / \underline{S}_{i,y} \rceil. \quad (2b)$$

² According to our tuned stitch sizes, the top and bottom layer skin can stretch up to 177% of their original length horizontally and up to 145% vertically. To obtain reasonable conductivity on the conductive stripes, the top and bottom layer skin must be stretched to at least 145% of their original length horizontally. There is no such limitation on the vertical axis, though. The implication here is that for the top and bottom layers, the range of 145% to 177% of the original length should contain H^{max} and H^{min} , and the range between 100% to 145% should contain V^{max} and V^{min} . For the mesh layer, there is no such limitations.

3. MODELING AND CALIBRATION

This section discusses how to calibrate both the location and the pressure response of the skin after installation. As shown in the calibration stage of Figure 1, the skin is stretched and can be slightly distorted when attached to the robot, making position calibration necessary to accurately determine the receptive field and force response of sensing cells. We accomplish this by repeatedly touching a fixed force torque sensor with the skin, as shown in the calibration stage of Figure 1. The entire process can be done automatically.

3.1 Data Collection for Calibration

To localize the skin and calibrate pressure measurement, we use an ATI Omega 85 force torque sensor attached to a fixed tripod (see calibration stage in Figure 1). Our aim is to obtain ground truth force torque signals for nearly every point on the skin. Data collection involves the robot approaching the sensor and actively touching it with the skin, generating a skin-traversal trajectory through Poisson-disc sampling on the target robot link's surface. The sample distance is half the grid size to ensure calibration of all cells during the run. The grid size is determined by the skin dimensions and the number of available analog Arduino pins (16 in our case using Arduino Mega 2560 Rev3). We allow for a maximum 26-degree angle between the force torque sensor and skin surface normal; and it is compensated through force vector projections. The order to traverse all points is optimized using a traveling salesman solver (Perron and Furnon) to minimize the calibration trajectory's make span. We collect timestamped tuples $(\forall i, C_{i,t}, F_t, P_t)$ at approximately 43 frames per second, where $i \in \mathbb{N}$ denotes the sensing cell, $C_{i,t} \in \mathbb{R}$ denotes the skin response at cell i at time t , $F_t \in \mathbb{R}$ represents the force torque sensor reading at time t , and $P_t \in \mathbb{R}^3$ indicates the force torque sensor position relative to the link origin at time t . Figure 3 illustrates an example data sequence.

3.2 Skin Localization

To determine the location of a sensing cell relative to the robot, we use a one-to-rest k-nearest neighbor classifier on the collected data. The k-nearest neighbor classifier has been shown to have robust performance in localizing the contact position of tactile sensors (Mohammadi et al., 2019). We apply a similar technique, but instead of determining the actual contact location, we calculate the receptive field of individual sensing cells based on the ground truth contact location given by the robot's forward kinematics.

The k-nearest neighbor algorithm calculates the weighted distance between the force torque sensor position P_t and the skin response $C_{i,t}$ of each sensing cell. We use weighted distance, where the weight assigned to each neighbor is inversely proportional to its distance from the query point, denoted as d_i . This is because our sampling points are sparse across the surface, and using weighted distance reduces the influence of noisy neighbors in the prediction. The prediction is then given as the class with the most votes from its k nearest neighbors.

$$\hat{y} = \arg \max_y \sum_{i=1}^k w_i \delta(y, y_i) \quad (3)$$

where $w_i = 1/d_i^2$ is the weight of the i^{th} nearest neighbor, and $\delta(y, y_i)$ is the indicator function that is 1 if $y = y_i$ and 0 otherwise.

We design k nearest neighbor classifiers for each cell. We selected $k = 1000$ as a hyperparameter since it provides the most robust outlier rejection. Each of the classifiers predicts whether a contact at a position in space could be detected by the cell. We then created an ensemble classifier which determines the receptive fields of each cell using majority voting. The classified cell boundaries and center locations are shown in Figure 4.

3.3 Pressure Calibration

After skin localization, the force response of each cell can be calibrated using linear regression of the data $\{(F_t, C_{i,t})\}$. We can find a linear function $f_i : C_{i,t} \mapsto F_t$ that best fits the data points for each sensing cell i by solving the following least square problem:

$$\min_{f_i} \sum_{t, \text{ s.t. } i_t=i} (f_i(C_{i,t}) - y_t)^2. \quad (4)$$

Figure 4 presents two plots representing the calibration outcomes for contact and force. We assessed our calibration model’s performance by splitting the dataset into a 90% training set and a 10% testing set, with the plots depicting the test error. The first plot showcases contact localization results, using the receptive field centroids of each cell to predict contact location based on cell output. Our testing set yielded a contact localization root mean square error (RMSE) of 3.00 cm. Before calibration, while assuming the skin is a perfect grid, the RMSE is 5.83 cm. Note that the localization error is limited by the grid sizes of the cells, which the mean side lengths of all cells is 2.89 cm. The second plot illustrates force calibration results, employing linear models for each cell to predict force based on cell voltage. The testing set exhibited a force prediction RMSE of 1.36 N, which is an improvement over naive scaling of skin readings based on cell’s saturation force where the RMSE is 1.92 N.

4. CONTROL APPLICATIONS

This section discusses how to use the skin to facilitate robot learning from human contacts, as shown in Figure 5. The skin-enabled controller uses contact force and position readings to calculate control displacements, which directly adjust robot behavior and provide rich signals for robot learning tasks. This process could allow for interactive responses to human contact and improve the overall effectiveness of human-robot interaction. The learning model is sensor-agnostic and has been studied by Shek et al. (2023). This section mainly focuses on the skin-enabled controller, with the integration of the learning model left for future work.

We provide two example design of the skin enabled controllers: 1) one controller that modifies robot trajectories using human contact signals and 2) one controller

that regulates force interactions between human and robot using tactile skins.

The experiments were conducted using the FANUC LR Mate 200iD/7L robot arm. We fabricated two rectangular skins for the second and fourth links, whose top layers measured 330 mm (width) by 363 mm (height) and 455 mm (width) by 140 mm (height), respectively. Each skin had an array of sensing cells, with the first skin containing a 16×16 array and the second skin containing a 16×8 array. The signals from each sensing cell were routed to an Arduino board, which then transmitted the signals to the controller via Ethernet. The transmission rate was 43 frames per second for the 16×16 skin and 74 frames per second for the 16×8 skin. The bandwidth of skin signals is limited by the hardware and will be addressed in future work. The control command was computed and sent to the robot via the stream motion interface at a rate of 125 Hz.

4.1 Trajectory Modification from Human Feedback

In this use case, we consider the situation when the human pushes the robot away from potentially dangerous configurations while the robot is following a Cartesian trajectory. Skin-enabled controllers can efficiently detect the contact position and generate new trajectories that minimize disruption to the robot’s original motion. Inspired by the collision avoidance algorithm in Lin et al. (2017), we formulate the trajectory modification problem as a quadratic program (QP). The objective of this QP formulation is to minimize the velocity difference between the original and modified trajectories while ensuring that the robot follows human’s commands. At the current joint configuration $q \in \mathbb{R}^6$, the velocity command $\dot{q}_{cmd} \in \mathbb{R}^6$ is computed by:

$$\begin{aligned} \min_{\dot{q}_{cmd}} \quad & \|\dot{x}_{ref} - J(q)\dot{q}_{cmd}\|_2^2 \\ \text{s.t.} \quad & u_i^\top J_i \dot{q}_{cmd} \geq f(F_i), \forall i \end{aligned} \quad (5)$$

where $J \in \mathbb{R}^{3 \times 6}$ is the Jacobian matrix associated with the end effector e at robot configuration q , $\dot{x}_{ref} \in \mathbb{R}^{3 \times 1}$ is the reference velocity of the end effector, $u_i \in \mathbb{R}^{3 \times 1}$ is the unit vector pointing away from the contact point i , and $J_i \in \mathbb{R}^{3 \times 6}$ is the Jacobian matrix evaluated at the contact point i , $f(F_i)$ is a non-negative and monotonic function that depends on the contact force at contact point i . When $f(F_i) \equiv 0$, the constraint is simply requiring that there is no motion against human touch. When $f(F_i) \propto F_i$, the robot will be pushed further away if the human pushes harder. The dimension of the constraint is the same as the number of contacts. Note that this formulation is different from Lin et al. (2017) in the following aspects: 1) (5) allows contact while Lin et al. (2017) avoids contact; 2) the magnitude of the constraint in (5) can be dependent on the magnitude of the contact force, while Lin et al. (2017) considers constant constraints in all situations, i.e., $f(F_i) \equiv 0$.

To demonstrate the effectiveness of (5), we conducted the following experiment when setting $f(F_i) \equiv 0$. The robot’s reference trajectory is to move its end effector from the bottom left to the top right, as shown in Figure 6. When human touches the robot, the skin successfully localized the point of contact to the 184th sensor cell, and

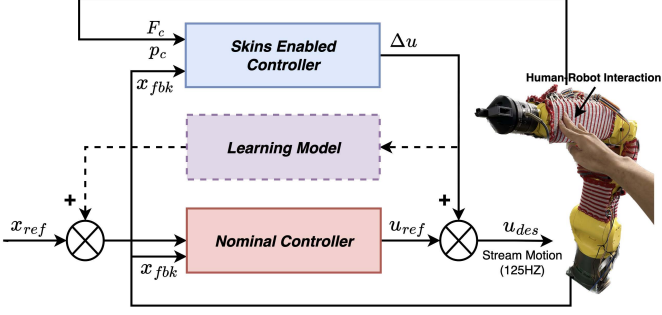


Fig. 5. The proposed skin-based control and learning framework.

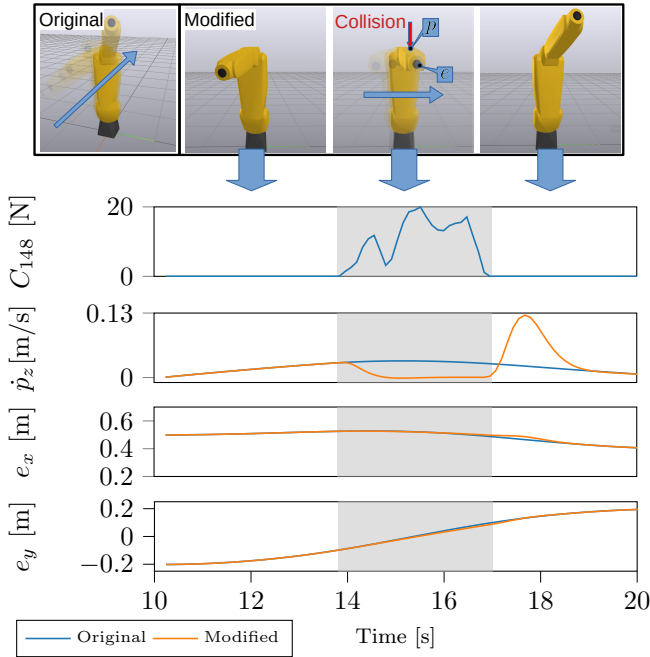


Fig. 6. Demonstration of trajectory modification from human feedback. The robot was programmed to move diagonally from the bottom left to the top right. In the first plot, it can be seen that a contact occurred between 13.8s and 17s. During the contact, the skin-enabled controller accurately localized the contact point at the top of the robot and reduced the velocity of the contact point to 0 in the z-direction (shown as p_z in the second plot). The original trajectory of the robot at the end effector was maintained in the x and y directions, namely e_x and e_y , as shown in the third and fourth plots respectively.

the robot's trajectory was immediately modified to reduce the Cartesian velocity in the direction of the contact to zero. Extensive evaluation of the proposed algorithm in (5) will be left for future work.

4.2 Skin-Enabled Admittance Control

This use case discusses how to let the robot generate desired force feedback to the human during contact, which is an important capability during human-robot interactions (Shek et al., 2023). However, prior works only utilized joint torque sensors, which can not localize the contact location, hence unable to correctly regulate the contact

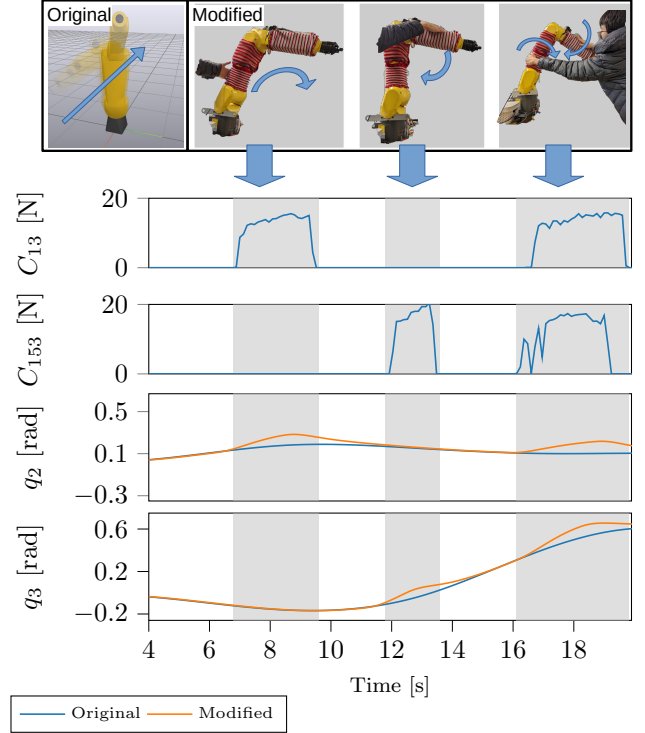


Fig. 7. Demonstration of robot admittance control with the skin. The robot moves from the bottom left to the top right, while the human operator intervenes at different stages. The lower portion of the robot is pushed from the back at first, followed by pressing the top link downwards, and finally simultaneous pushing and pressing. The three intervention stages are highlighted in gray. This scenario involves multiple joints and contacts between the human and robot. The results indicate that interactions with the top link (triggering C_{153} and moving q_3) and the lower link (triggering C_{13} and moving q_2) can be performed independently of each other.

force. Skin-enabled admittance control solves this limitation by dynamically regulate the forces applied to the contact point (Pugach et al. (2016)). The corresponding dynamic equation is:

$$M\Delta\ddot{x}(t) + B\Delta\dot{x}(t) + K\Delta x(t) = F_i(t) \quad (6)$$

where $\Delta x(t)$ is the contact point displacement, $\Delta\dot{x}(t)$ and $\Delta\ddot{x}(t)$ are its first and second derivatives, $F_i(t)$ denotes the measured contact force from the skin. The parameters M (inertia), B (damping coefficient), and K (stiffness) are design parameters to be selected case-by-case.

As the robot system operates on a discrete domain, admittance control law in (6) is converted from time domain to Z domain using Laplace transform and Tustin's approximation (Lahr et al., 2016). The admittance control displacements at time step k is:

$$\Delta x(k) = [T_s^2 F_i(k) + 2T_s^2 F_i(k-1) + T_s^2 F_i(k-2) - (2KT_s^2 - 8M)\Delta x(k-1) - (4M - 2BT_s^2 + KT_s^2)\Delta x(k-2)] * 1/[4M + 2BT_s^2 + KT_s^2] \quad (7)$$

where T_s is the sample time of the control loop.

The algorithm (7) is tested on the FANUC LR Mate 200id/7L industrial robot with $K = 500N/rad$, a critically damped damping parameter of $B = 2\sqrt{K}$, and $M = 0$. Unlike joint torque sensors, which cannot distinguish forces applied to different joints in the multi-joint, multi-contact case, the skin-enabled admittance control measure contact force and location on the robot surface and allows each joint to respond independently to contacts. Figure 7 illustrates this capability. With skin-enabled admittance control, the interactive force profiles between humans and robots are smoother (compared to Fig. 6). The human operator can interact with the robot in a more intuitive manner and provide rich contact information for learning from human feedback.

It is worth noting that since admittance control works by adding the displacement of the robot state to the reference trajectory, and the tactile skin could sense multi-touch, a joint could respond to multiple contacts on a single joint. The desired robot trajectory in multi-contact scenarios can be calculated by equation (8). Testing of the algorithm will be left for future work.

$$x_{des}(k) = x_{ref}(k) + \Delta x_{c1}(k) + \Delta x_{c2}(k) + \dots + \Delta x_{cN}(k). \quad (8)$$

5. CONCLUSION

This work presents a comprehensive solution for rapidly fabricating, calibrating, and deploying textile and tactile skins for interactive industrial robots. We developed an automated skin calibration method that enables simultaneous calibration of contact force and locations for different robots, making it more efficient to deploy these skins in various industrial settings. Furthermore, we demonstrated the effectiveness of textile and tactile skins in control applications, which can help improve human-robot interaction and learning in real-world scenarios.

Our experimental results showed that calibrated textile and tactile skins can effectively sense contact locations and forces, demonstrating the potential of these skins as a valuable sensing modality for enhancing robot learning and control. For future work, we plan to streamline the calibration process for multiple skins and develop an integrated skin for multiple robot links. We also aim to utilize the vast information collected from the skin during human-robot interactions for more complex robot learning applications.

ACKNOWLEDGEMENTS

This research is supported by the CMU Manufacturing Futures Institute, made possible by the Richard King Mellon Foundation.

REFERENCES

Baykas, P.B., Bayraktar, E., and Yigit, C.B. (2020). Safe human-robot interaction using variable stiffness, hyper-redundancy, and smart robotic skins. In *Service Robotics*. IntechOpen.

Cao, M.Y., Laws, S., and y Baena, F.R. (2021). Six-axis force/torque sensors for robotics applications: A review. *IEEE Sensors Journal*, 21(24), 27238–27251.

Cirillo, A., Ficuciello, F., Natale, C., Pirozzi, S., and Villani, L. (2015). A conformable force/tactile skin for physical human–robot interaction. *IEEE Robotics and Automation Letters*, 1(1), 41–48.

Dahiya, R.S., Mittendorfer, P., Valle, M., Cheng, G., and Lumelsky, V.J. (2013). Directions toward effective utilization of tactile skin: A review. *IEEE Sensors Journal*, 13(11), 4121–4138.

Fan, X., Lee, D., Jackel, L., Howard, R., Lee, D., and Isler, V. (2022). Enabling low-cost full surface tactile skin for human robot interaction. *IEEE Robotics and Automation Letters*, 7(2), 1800–1807.

Kloss, A., Bauza, M., Wu, J., Tenenbaum, J.B., Rodriguez, A., and Bohg, J. (2020). Accurate vision-based manipulation through contact reasoning. In *2020 IEEE International Conference on Robotics and Automation (ICRA)*, 6738–6744. IEEE.

Lahr, G.J., Soares, J.V., Garcia, H.B., Siqueira, A.A., and Caurin, G.A. (2016). Understanding the implementation of impedance control in industrial robots. In *2016 XIII Latin American Robotics Symposium and IV Brazilian Robotics Symposium (LARS/SBR)*, 269–274. IEEE.

Lin, H.C., Liu, C., Fan, Y., and Tomizuka, M. (2017). Real-time collision avoidance algorithm on industrial manipulators. In *2017 IEEE Conference on Control Technology and Applications (CCTA)*, 1294–1299. doi: 10.1109/CCTA.2017.8062637.

Mohammadi, A., Xu, Y., Tan, Y., Choong, P., and Oetomo, D. (2019). Magnetic-based soft tactile sensors with deformable continuous force transfer medium for resolving contact locations in robotic grasping and manipulation. *Sensors*, 19(22). doi:10.3390/s19224925. URL <https://www.mdpi.com/1424-8220/19/22/4925>.

Perron, L. and Furnon, V. (????). Or-tools. URL <https://developers.google.com/optimization/>.

Pugach, G., Melnyk, A., Tolochko, O., Pitti, A., and Gaussier, P. (2016). Touch-based admittance control of a robotic arm using neural learning of an artificial skin. In *2016 IEEE/RSJ International Conference on Intelligent Robots and Systems (IROS)*, 3374–3380. doi: 10.1109/IROS.2016.7759519.

Shek, A., Chen, R., and Liu, C. (2023). Learning from physical human feedback: An object-centric one-shot adaptation method. *arXiv preprint arXiv:2203.04951*.

Si, Z., Yu, T.C., Morozov, K., McCann, J., and Yuan, W. (2023). Robotswearer: Scalable, generalizable, and customizable machine-knitted tactile skins for robots. *arXiv preprint arXiv:2303.02858*.

Touch Solution (2023). Touch solution. <https://www.touche.solutions>. Accessed: April 10, 2023.

Tsuji, S. and Kohama, T. (2020). A general-purpose safety light curtain using tof sensor for end effector on human collaborative robot. *IEEJ Transactions on Electrical and Electronic Engineering*, 15(12), 1868–1874.

Wahrburg, A., Bös, J., Listmann, K.D., Dai, F., Matthias, B., and Ding, H. (2017). Motor-current-based estimation of cartesian contact forces and torques for robotic manipulators and its application to force control. *IEEE Transactions on Automation Science and Engineering*, 15(2), 879–886.